BIOCHEMISTRY
including biophysical chemistry & molecular biology

Article

pubs.acs.org/biochemistry

Biochemical and Structural Characterization of the *trans*-Enoyl-CoA Reductase from *Treponema denticola*

Brooks B. Bond-Watts,[†] Amy M. Weeks,[†] and Michelle C. Y. Chang*[,†,‡]

[†]Department of Chemistry and [‡]Department of Molecular and Cell Biology, University of California, Berkeley, California 94720-1460, United States

Supporting Information

ABSTRACT: The production of fatty acids is an important cellular pathway for both cellular function and the development of engineered pathways for the synthesis of advanced biofuels. Despite the conserved reaction chemistry of various fatty acid synthase systems, the individual isozymes that catalyze these steps are quite diverse in their structural and biochemical features and are important for controlling differences at the cellular level. One of the key steps in the fatty acid elongation cycle is the enoyl-ACP (CoA) reductase function that drives the equilibrium forward toward chain extension. In this work, we report the structural and biochemical characterization of the *trans*-enoyl-CoA reductase from *Treponema denticola* (tdTer), which has been utilized for the engineering of synthetic biofuel pathways with an order of magnitude increase in product titers compared to those of pathways constructed with other enoyl-CoA reductase components. The crystal structure of tdTer was determined to 2.00 Å resolution and shows that the Ter enzymes are distinct from members of the FabI, FabK, and FabL families but are highly similar to members of the FabV family. Further biochemical studies show that tdTer uses an ordered bi-bi mechanism initiated by binding of the NADH redox cofactor, which is consistent with the behavior of other enoyl-ACP (CoA) reductases. Mutagenesis of the substrate binding loop, characterization of enzyme activity with respect to crotonyl-CoA, hexenoyl-CoA, and dodecenoyl-CoA substrates, and product inhibition by lauroyl-CoA suggest that this region is important for controlling chain length specificity, with the major portal playing a more important role for longer chain length substrates.

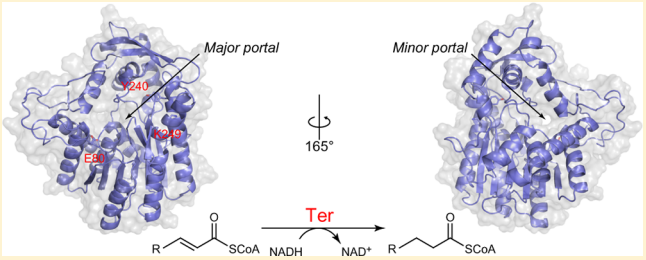

The construction of hydrocarbon backbones through the fatty acid metabolic machinery plays a key role in cellular maintenance[1,2] as well as in the development of engineered pathways for the production of advanced biofuels.[3−8] Although the chemistry of fatty acid synthesis is highly conserved, there is a range of diversity in the enzyme systems that catalyze these reactions that is important for their physiological function.[9−12] Indeed, the choice between individual FAS components with different biochemical behavior is important at the cellular level for controlling product titers from engineered biofuel pathways. For example, the switch from the native flavin-dependent enoyl-CoA reductase used in the production of *n*-butanol, a key second-generation biofuel, to a flavin-independent *trans*-enoyl-CoA reductase from *Treponema denticola* (tdTer)[13] leads to an order of magnitude increase in product yield in engineered *Escherichia coli*.[14,15] Interestingly in this case, the Ter appears to allow the pathway flux to be driven forward without the use of malonyl-CoA and ATP by introducing a kinetic trap at the enoyl-CoA reduction step.[14]

The Ter family of reductases was first identified from *Euglena gracilis* (egTer), a photosynthetic algae with five different FAS systems, including a type II malonyl-CoA-independent pathway in the mitochondria that uses CoA rather than ACP as the acyl carrier.[16−19] The egTer enzyme was isolated and characterized from *E. gracilis* mitochondrial extracts and was proposed to serve as the enoyl-CoA reductase in this system.[20,21] In terms of phylogeny, Ters are distinct from members of the FabI family, which represents the major enoyl-ACP reductase used in type II FAS systems, as well as from the FabK and FabL isozymes.[9,10] However, they are quite similar to FabV enzymes, which is a relatively recently discovered class of enoyl-ACP reductases that was discovered in *Vibrio cholerae*.[22] On the basis of the ability of Ters to amplify fuel titers in engineered CoA-linked pathways, we set out to further structurally and biochemically characterize tdTer. We now report the crystal structure of tdTer as well as mutagenesis studies to examine the function of the substrate binding loop in determining chain length specificity.

MATERIALS AND METHODS

Commercial Materials. Terrific Broth (TB), LB Broth Miller (LB), LB Agar Miller, reagent grade triethylamine (TEA), and glycerol were purchased from EMD Biosciences (Darmstadt, Germany). Isopropyl β-D-1-thiogalactopyranoside (IPTG), D-glucose, dithiothreitol (DTT), phenylmethanesul-

Received: June 30, 2012
Revised: August 7, 2012
Published: August 20, 2012

   dx.doi.org/10.1021/bi300879n | *Biochemistry* 2012, 51, 6827−6837

fonyl fluoride (PMSF), sodium phosphate, sodium chloride, streptomycin sulfate, Tris-HCl, Tris base, hydrogen chloride, sodium hydroxide, high-performance liquid chromatography (HPLC) grade methylene chloride, HPLC grade acetonitrile, and carbenicillin (Cb) were purchased from Fisher Scientific (Pittsburgh, PA). Crotonyl-CoA, butyryl-CoA, hexanoyl-CoA, lauroyl-CoA, *trans*-2-hexenoic acid, coenzyme A hydrate, *N*,*N*-dimethylformamide (DMF), ethyl chloroformate, *N*,*N*,*N*,*N*-tetramethylethylenediamine (TEMED), NADH, NADPH, NAD^+, and $NADP^+$ were purchased from Sigma-Aldrich (St. Louis, MO). *trans*-2-Dodecenoic acid was purchased from Oakwood Products, Inc. (West Columbia, SC). Imidazole and formic acid were purchased from Acros Organics (Geel, Belgium). Potassium bicarbonate was purchased from Mallinckrodt (St. Louis, MO). Polyacrylamide (30%, 37.5:1), electrophoresis grade sodium dodecyl sulfate (SDS), and ammonium persulfate were purchased from Bio-Rad Laborabories (Hercules, CA). PageRuler Plus Prestained Protein Ladder and DNase were purchased from Fermentas (Glen Burnie, MD). Deoxynucleotides (dNTPs) and Platinum Taq High-Fidelity polymerase (Pt Taq HF) were purchased from Invitrogen (Carlsbad, CA). Complete Protease Inhibitor tablets were purchased from Roche Applied Science (Indianapolis, IN). All restriction enzymes, antarctic phosphatase, and T4 DNA ligase were purchased from New England Biolabs (Ipswich, MA). Phusion polymerase was purchased from Finnzymes (Lafayette, CO). Ni-NTA agarose resin was purchased from Qiagen (Valencia, CA). pET16b was purchased from Novagen (San Diego, CA). Oligonucleotides were purchased from Integrated DNA Technologies (Coralville, IA) and resuspended at a stock concentration of 100 μM in 10 mM Tris-HCl (pH 8.5). DNA was isolated using the QIAprep Spin Miniprep Kit, QIAquick PCR Purification Kit, and QIAquick Gel Extraction Kit (Qiagen) as appropriate. All absorbance readings were taken on a DU-800 spectrometer (Beckman-Coulter, Fullerton, CA) or a SpectraMax M2 plate reader (Molecular Devices, Toronto, ON). RP-HPLC purifications were performed on an Agilent 1200 series HPLC system coupled to a diode-array detector. Liquid chromatography−mass spectrometry data were collected on an Agilent 1290 series instrument. High-resolution mass spectral analyses were conducted at the College of Chemistry Mass Spectrometry Facility.

Bacterial Strains. *E. coli* DH10B-$T1^R$ (Invitrogen) and BL21(de3)-$T1^R$ (New England Biolabs) were used for the construction of plasmids and protein production, respectively.

Phylogenetic Analysis. Using sequences of characterized Ter (*T. denticola*[13] and *E. gracilis*[21]) and FabV enzymes (from *V. cholerae*,[22] *Burkholderia mallei*,[23] *Pseudomonas aeruginosa*,[24] *Xanthomonas orzyae*,[25] and *Yersinia pestis*[26]) as well as FabI from *E. coli*, the UniRef50 database[27,28] was searched to yield sequences that are less than 50% identical. For each homology search, the top 10 scoring entries were selected. All identified sequences were compiled, redundant sequences were removed, and the sequences were aligned with MEGA 5[29] using the MUSCLE algorithm.[30] The alignment output was analyzed over 394 positions using the maximum likelihood method in MEGA with a nearest-neighbor-interchange strategy, while allowing for deletion of gaps that exist in less than 50% of the sequences and 500 bootstrap replicates to evaluate the confidence.

Construction of Plasmids. pET16b-His_{10}-Ter was constructed by amplification of the synthetic *ter* gene with the TdTer F1 and TdTer R101 primers and insertion into the NdeI-XhoI restriction sites of pET16b. The Y240F mutant was constructed by splicing by overlap extension polymerase chain reaction using standard methods with TdTer F1/TdTer SOE R1 (5′-end) and TdTer SOE F1/TdTer R101 (3′-end) and inserted into the NdeI−XhoI restriction sites of pET16b (Table S1 of the Supporting Information). All other mutants were generated by site-directed mutagenesis using Quikchange (Table S1 of the Supporting Information). pET23a-His_{10}-Tev-Ter was constructed by amplification of the synthetic *ter* gene with the TdTer F102 and TdTer R101 primers and insertion into the SfoI−XhoI restriction sites of a pET23a derivative, which was modified to encode a His_{10} tag and TEV protease cleavage site (Macrolab, University of California, Berkeley, CA). All plasmids were verified by sequencing following construction (Quintara Biosciences, Albany, CA).

Expression of Ter Variants. TB containing carbenicillin (50 μg/mL) was inoculated to an OD_{600} of 0.05 with an overnight TB culture of *E. coli* BL21(de3)-$T1^R$, freshly transformed with the expression plasmid. The cultures were grown at 37 °C and 200 rpm to an OD_{600} of 0.6−0.8 before induction with IPTG (1 mM) and a decrease in the temperature to 30 °C. Cells were harvested 4 h after IPTG addition by centrifugation at 12300*g* for 7 min at 4 °C and stored at −80 °C.

Expression of Selenomethionine His_{10}-Tev-Ter. LB containing carbenicillin (50 mL, 50 μg/mL) was inoculated to an OD_{600} of 0.05 with an overnight LB culture of *E. coli* BL21(de3)-$T1^R$, freshly transformed with pET23a-His_{10}-Tev-Ter. The cultures were grown at 37 °C and 200 rpm to an OD_{600} of 0.6−0.8. The culture was spun down (12300*g* for 7 min) and washed in 50 mL of M9-MOPS medium [1× M9 salts, 100 mM MOPS (pH 7.4), 1% D-glucose, 2 mM $MgSO_4$, 0.1 mM $CaCl_2$, 0.1 μg/mL thiamine, 10 μM ferrous sulfate, 0.1 μM zinc sulfate, 0.8 μM manganese chloride, 0.15 μM cupric sulfate, 0.3 μM cobalt chloride, 4 μM boric acid, and 30 nM ammonium molybdate] containing carbenicillin (50 μg/mL). The cells were centrifuged (12300*g* for 7 min) and resuspended in M9-MOPS Cb medium (50 mL). One liter of prewarmed (37 °C) M9-MOPS Cb medium was then inoculated with the cell suspension (10 mL). The culture was grown at 37 °C and 200 rpm to an OD_{600} of 0.4−0.8 and supplemented with a filter-sterilized amino acid mixture (leucine, isoleucine, and valine, final concentration of 50 mg/L; phenylalanine, lysine, and threonine, final concentration of 100 mg/L; selenomethionine, final concentration of 75 mg/L). After an additional incubation at 15 min, the cells were cooled on ice while being shaken for 30 min before induction with IPTG (1 mM). The culture was then grown overnight (12−16 h) at 16 °C and 200 rpm. Cells were harvested by centrifugation at 12300*g* for 7 min at 4 °C and stored at −80 °C.

Purification of Ter Variants. The cell pellet was thawed and resuspended at a level of 5 mL/g of cell pellet in buffer A [50 mM sodium phosphate, 300 mM sodium chloride, and 20 mM imidazole (pH 8.0) at 4 °C] containing PMSF (500 μM) and DNase (0.7 unit/g of cell pellet). The cells were homogenized prior to lysis by being passed through a French pressure cell (Thermo Scientific) at 14000 psi. The total lysate was centrifuged at 12300*g* for 45 min at 4 °C to separate the soluble and insoluble fractions. The DNA was precipitated from the cleared cell lysate with streptomycin sulfate [20% (w/v)] added dropwise over 10 min at 4 °C to a final concentration of 1%. The precipitated DNA was removed by centrifugation at

12300*g* for 30 min at 4 °C. The supernatant was loaded onto a Ni-NTA agarose column (3−5 mL) using an ÄKTA Purifier FPLC system (GE Healthcare) at a flow rate of 0.5 mL/min. The column was washed at a flow rate of 2 mL/min with 20 column volumes (cv) of buffer A followed by 20 cv of 92% buffer A and 8% buffer B [50 mM sodium phosphate, 300 mM sodium chloride, and 250 mM imidazole (pH 8.0) at 4 °C]. The column was eluted with buffer B. Protein-containing fractions were identified and pooled by their absorbance at 280 nm and used for downstream purification as described below. The concentration of purified protein was estimated using the extinction coefficient at 280 nm calculated by the ExPASy Peptide Properties Calculator for His_{10}-Ter (42560 M^{-1} cm^{-1}).

His_{10}-Ter Variants. The pooled fractions from the Ni-NTA agarose column were concentrated to <5 mL using an Amicon stirred ultrafiltration cell with an Ultracel 5000 molecular weight cutoff (MWCO) filter membrane (Millipore), loaded onto a G-25 column (100 mL), and eluted with buffer C [20 mM Tris-HCl and 50 mM sodium chloride (pH 7.5) at 4 °C]. The protein-containing fractions were identified and pooled by their absorbance at 280 nm. After concentration to ∼5 mg/mL, glycerol (60% stock solution) was added to a final concentration of 5% (v/v). Proteins were then flash-frozen in liquid nitrogen and stored at −80 °C.

GTGA-Ter. The pooled fractions from the Ni-NTA agarose column were concentrated to <3 mL as previously described. TEV protease (1 mg of TEV/50 mg of Ter) and DTT (1 mM) were added, and the mixture was dialyzed at 4 °C for 16 h against TEV cleavage buffer [3.5 L; 50 mM sodium phosphate, 300 mM sodium chloride, and 1 mM DTT (pH 8.0)] using 3500−5000 MWCO cellulose ester tubing. To remove the His_{10}-tagged TEV protease and the His_{10} peptide, the dialysate was passed over the washed (20 cv of buffer A) Ni-NTA agarose column. The column flow-through and an additional wash (1 cv of buffer A) were collected and concentrated to 2 mL using a 3000 MWCO Amicon Ultra-15 apparatus. The concentrated protein was loaded onto a HiLoad 16/60 Superdex 75 prep grade column (GE Healthcare) using an ÄKTA Purifier FPLC system (1 mL/min). GTGA-Ter was eluted with buffer C and concentrated to 30−60 mg/mL for immediate use in crystallization. For purification of selenomethionine GTGA-Ter, all solutions were supplemented with TCEP (0.5 mM).

Size-Exclusion Chromatography. Ter variants (∼0.5 mg) were analyzed on a HiLoad 16/60 Superdex 200 prep grade column (GE Healthcare) using an ÄKTA Purifier FPLC system (1 mL of buffer C/min, 500 μL sample loop). The elution volume:void volume ratio was compared to those of the standard proteins (Bio-Rad). Protein molecular weight was estimated by fitting the data using Excel (Microsoft, Redmond, WA) to the equation $\log_{10} MW = m \times V_e/V_o + b$, where MW is the molecular weight, V_e is the elution volume, and V_o is the void volume.

Crystallization and Structure Determination of GTGA-Ter. Protein crystals were obtained using the hanging drop vapor diffusion method by combining equal volumes of a protein solution (diluted to 20 mg/mL) and a reservoir solution [0.1 M sodium citrate (pH 7.5), 25% polyethylene glycol 6000, and 2.5% glycerol]. Crystals grew within 2 days and were cryoprotected by being briefly soaked in a solution containing 75% reservoir solution and 25% ethylene glycol followed by flash-freezing in liquid nitrogen. Data were collected at Beamline 8.3.1 at the Advanced Light Source (Lawrence Berkeley National Laboratory, Berkeley, CA). Data sets for native crystals were collected at a wavelength of 1.116 Å, while selenomethionine-modified Ter crystals were analyzed with an inflection/peak wavelength of 0.979 Å and remote wavelength of 0.957 Å. Data sets were processed and merged with XDS and XSCALE. Experimental phases were determined from the location of selenium atoms using Phenix AutoSol[31] and used to build an initial model for selenomethionine-modified Ter with Phenix AutoBuild. This model was then used to determine the structure of the native protein by molecular replacement using Phenix AutoMR and AutoBuild to build a near-complete chain trace of each crystal. Iterative cycles of Phenix AutoRefine and manual refinement in Coot[32] were used to generate the final model. Cocrystallization with stoichiometric amounts of substrates and/or products (NADH, NAD^+, NAD^+/crotonyl-CoA, and NAD^+/butyryl-CoA) was tested, but insufficient electron density was observed to create a model for any bound ligand.

Modeling Substrates. The docking model was generated using Glide SP[33−35] in the Maestro molecular visualization environment. Each substrate was first optimized and minimized without taking into account nonpolar hydrogens using the Maestro Preparation Wizard. The NADH was docked first as a flexible ligand in the tdTer chain A active site in 20 poses by generating a scoring grid (size, 20 Å × 20 Å × 20 Å; ligand search range, 14 Å × 14 Å × 14 Å) encompassing the entire active site and correlated with the location of the bound NADH in the *Y. pestis* FabV crystal structure [Protein Data Bank (PDB) entry 3ZU3].[26] The top five poses were analyzed, and the docking model most closely resembling the *Y. pestis* FabV crystal structure was used to generate a receptor grid (size, 20 Å × 20 Å × 20 Å; ligand search range, 14 Å × 14 Å × 14 Å) centered around Y240 to dock the crotonyl-CoA substrate using the same approach.

Synthesis of Acyl-CoAs. Acyl-CoAs were prepared using the mixed anhydride method.[36] Briefly, *trans*-2-hexenoic acid or *trans*-2-dodecenoic acid (52 μmol) was preincubated with triethylamine (1 equiv, 52 μmol, 7.3 μL) for 30 min at room temperature in CH_2Cl_2 (1 mL). The reaction mixture was then cooled to 4 °C before the addition of ethyl chloroformate (1 equiv, 52 μmol, 5.0 μL). After incubation for 2 h, CH_2Cl_2 was evaporated from the reaction mixture with N_2 at 4 °C. The residue was resuspended in DMF (1.5 mL), transferred into a stirred solution of coenzyme A hydrate (0.5 equiv, 26 μmol, 20 mg) in 0.4 M potassium bicarbonate (pH 8.4, 1.5 mL), and incubated at room temperature for 10 min. The reaction mixture was then acidified to pH 3−4 with formic acid, diluted to 50 mL with water, flash-frozen with liquid N_2, and lyophilized. After resuspension in water (1 mL), the acyl-CoA was purified by RP-HPLC on an Eclipse XDB C-18 column (5 μm, 9.4 mm × 250 mm, Agilent) using a linear gradient from 0 to 50% acetonitrile over 18 min with water as the aqueous mobile phase (3 mL/min). The fractions containing product were pooled and lyophilized.

trans-2-Hexenoyl-CoA. The >85% pure fractions were pooled and repurified by RP-HPLC to yield a >95% pure product: ^{1}H NMR (600 MHz, D_2O, 25 °C) δ (alkyl chain numbered as C_{X^*} from carbonyl) 8.52 (s, 1H, H_8), 8.22 (s, 1H, H_2), 6.89 (m, 1H, C_{3^*}), 6.13 (m, 2H, $H_{1'}$ and C_{2^*}), 4.57 (m, 1H, $H_{4'}$), 4.21 (m, 2H, $H_{5'}$), 4.00 (s, 1H, $H_{3''}$), 3.82 (m, 1H, $H_{1a''}$), 3.53 (m, 1H, $H_{1b''}$), 3.41 (t, J = 6.6 Hz, 2H, $H_{5''}$), 3.31 (t, J = 6.3 Hz, 2H, $H_{8''}$), 2.99 (t, J = 6.3 Hz, 2H, $H_{9''}$), 2.39 (t, J = 6.6 Hz, 2H, $H_{6''}$), 2.13 (q, J = 7.2 Hz, 2H, C_{4^*}), 1.41 (sex, J =

dx.doi.org/10.1021/bi300879n | *Biochemistry* 2012, 51, 6827−6837

7.3 Hz, 2H, C_{5*}), 0.85 (m, 6H, $H_{10''}$ and C_{6*}), 0.73 (s, 3H, $H_{11''}$); ^{13}C NMR (600 MHz, D_2O, 25 °C) δ (alkyl chain numbered as C_{X*} from carbonyl) 193.86 (C_{1*}), 174.73 ($C_{7''}$), 174.00 ($C_{4''}$), 155.67 (C_6), 152.60 (C_2), 149.32 (C_4), 148.59 (C_8), 139.89 (C_{3*}), 127.81 (C_{2*}), 118.63 (C_5), 86.34 ($C_{1'}$), 83.52 ($C_{4'}$), 74.23 ($C_{2'}$), 74.20 ($C_{3'}$), 74.09 ($C_{3''}$), 73.80 ($C_{1''}$), 71.86, 65.35 ($C_{5''}$), 38.63 ($C_{8''}$), 38.31 ($C_{2''}$), 38.26, 35.38 ($C_{5''}$), 35.31 ($C_{6''}$), 33.67 (C_{4*}), 27.74 ($C_{9''}$), 20.83 ($C_{10''}$), 20.50 (C_{5*}), 18.11 ($C_{11''}$), 12.86 (C_{6*}); HR-ESIMS $(M - 2H)^{2-}$ calcd for $C_{27}H_{42}O_{17}N_7P_3S$ m/z 430.5791, found m/z 430.5787.

trans-2-Dodecoyl-CoA. The >95% pure fractions were pooled and used for enzyme assays: ^{1}H NMR (600 MHz, D_2O, 25 °C) δ (alkyl chain numbered as C_{X*} from carbonyl) 8.54 (s, 1H, H_8), 8.24 (s, 1H, H_2), 6.92 (m, 1H, C_{3*}), 6.14 (m, 2H, $H_{1'}$ and C_{2*}), 4.58 (m, 1H, $H_{4'}$), 4.23 (m, 2H, $H_{5'}$), 4.02, (s, 1H, $H_{3''}$), 3.84 (m, 1H, $H_{1a''}$), 3.76 (m, 1H), 3.63 (m, 1H, $H_{1b''}$), 3.54 (m, 2H), 3.43 (t, J = 6.6 Hz, 2H, $H_{5''}$), 3.35 (t, J = 6.6 Hz, 2H, $H_{8''}$), 3.03 (t, J = 6.3 Hz, 2H, $H_{9''}$), 2.41 (t, J = 6.3 Hz, 2H, $H_{6''}$), 2.15 (q, J = 7.2 Hz, 2H, C_{4*}), 1.37 (sex, J = 7.3 Hz, 2H, C_{5*}), 1.18 (m, 12H, C_{6*}, C_{7*}, C_{8*}, C_{9*}, C_{10*}, C_{11*}), 0.88 (s, 3H, $H_{10''}$), 0.82 (t, J = 7.2 Hz, 3H, C_{12*}), 0.75 (s, 3H, $H_{11''}$); ^{13}C NMR (900 MHz, D_2O, 25 °C) δ (alkyl chain numbered as C_{X*} from carbonyl) 196.65 (C_{1*}), 184.63, 177.46 ($C_{7''}$), 176.74 ($C_{4''}$), 158.33 (C_6), 155.56 (C_2), 152.10 (C_4), 151.82 (C_8), 142.60 (C_{3*}), 130.54 (C_{2*}), 121.42 (C_5), 89.10 ($C_{1'}$), 86.31 ($C_{4'}$), 77.00 ($C_{2'}$), 76.88 ($C_{3'}$), 76.71 ($C_{3''}$), 74.83 ($C_{1''}$), 74.63, 68.11, 65.26 ($C_{5''}$), 41.42 ($C_{8''}$), 41.11 ($C_{2''}$), 38.23 ($C_{5''}$), 38.18 ($C_{6''}$), 34.37 ($C_{9''}$), 33.89 ($C_{10''}$), 31.32 (C_{4*}), 31.14 (C_{10*}), 31.11 (C_{6*}), 30.89 (C_{7*}), 30.58 (C_{5*}), 29.73 (C_{8*}), 26.47 (C_{9*}), 24.80 (C_{11*}), 23.66 ($C_{10''}$), 20.96 ($C_{11''}$), 16.19 (C_{12*}); HR-ESIMS $(M - 2H)^{2-}$ calcd for $C_{33}H_{54}O_{17}N_7P_3S$ m/z 472.6260, found m/z 472.6251.

Steady-State Kinetic Measurements. Ter activity was measured by monitoring the decrease in absorbance of NAD(P)H at 340 nm using a modified literature protocol.[14] The specific conditions used for each tdTer variant are available in the Supporting Information. Data were analyzed by nonlinear curve fitting to the Michaelis–Menten equation with data reported as mean ± the standard error ($n \geq 3$). The error in k_{cat}/K_M was calculated by error propagation from the individual kinetic constants.

Ternary Complex Formation. Assays were performed as described for steady-state kinetics. Data ($n \geq 3$) were plotted using a double-reciprocal plot and analyzed using least-squares regression linear fitting. Ten nanograms of His_{10}-Ter was used per reaction (250 μL). Crotonyl-CoA was used at concentrations of 5, 10, 25, 50, and 100 μM and NADH at concentrations of 3, 4, 5, 7.5, and 10 μM. All crotonyl-CoA concentrations were run at all NADH concentrations.

Order of Binding. Assays were performed as described for steady-state kinetics. The specific conditions for each reaction are available in the Supporting Information. Data ($n \geq 3$) were plotted using a double-reciprocal plot and analyzed using least-squares regression linear fitting to analyze product inhibition patterns by NAD^+ and butyryl-CoA. Twenty nanograms of His_{10}-Ter was used per reaction (250 μL).

Substrate Inhibition. Assays were performed as described for steady-state kinetics. Data ($n \geq 3$) were analyzed by nonlinear curve fitting to the Michaelis–Menten equation to obtain $V_{max,app}$ and $K_{M,app}$, which were used to calculate K_i and K_i'. The following substrate concentrations were used for His_{10}-Ter (20 ng, 250 μL): hexenoyl-CoA (10, 100, or 200 μM) or dodecenoyl-CoA (5, 10, or 15 μM) with 1.5, 2.5, 5, 10, 25, 37.5, 50, 100, or 200 μM NADH.

Product Inhibition. Assays were performed as described for steady-state kinetics. The specific conditions used for each tdTer variant are available in the Supporting Information. Data ($n \geq 3$) were analyzed by nonlinear curve fitting to the Michaelis–Menten equation to obtain $V_{max,app}$ and $K_{M,app}$.

RESULTS AND DISCUSSION

Phylogeny of *trans*-Enoyl-CoA Reductases. To examine the relationship between the Ter and functionally related FabV and FabI families, a phylogenetic tree was constructed using a maximum likelihood approach with 500 bootstrap replicates from a sequence alignment of the top 10 homologues from the UniRef50 database of two characterized Ter enzymes (*T. denticola*[13] and *E. gracilis*[21]), five characterized FabVs (*V. cholerae*,[22] *B. mallei*,[23] *P. aeruginosa*,[24] *X. orzyae*,[25] and *Y. pestis*[26]), as well as the FabI from *E. coli*[9,10] (Figure 1 and Figure S1 of the Supporting Information). Like the FabVs, Ters share little sequence identity with and are significantly larger in size than FabIs, which serve as the major enoyl-ACP reductase of canonical type II fatty acid synthase systems.[9,10] The Ter sequences were consequently found to cluster with FabVs on a separate branch compared to FabIs. In this analysis, the prokaryotic Ter enzyme from *T. denticola* (tdTer) lies on a different branch compared to that of the characterized FabVs (46–52% identical sequences); however, the eukaryotic Ter from *E. gracilis* (egTer) was found to cluster with the FabV branch (52–57% identical sequences with the functionally encoded protein). These observations suggest that Ter enzymes may potentially diverge from FabVs, but that the two families of reductases may overlap or be difficult to distinguish by sequence analysis or annotation alone.

Crystal Structure of the *trans*-Enoyl-CoA Reductase from *T. denticola*. On the basis of the distinct phylogeny of tdTer and the absence of any Ter crystal structures deposited in the Protein Data Bank, we set out to structurally characterize tdTer and to study its function in more detail. For structural studies, the synthetic gene encoding tdTer was heterologously expressed in *E. coli* with an N-terminal His_{10} tag and an intervening TEV protease site, which was removed to yield enzyme with a residual GTGA linker at the N-terminus (Figure S2 of the Supporting Information). tdTer crystallized in an asymmetric unit containing four identical copies of the Ter monomer, which is in agreement with the apparent molecular weight measured in solution (Figure S3 of the Supporting Information). Until the recent deposit of the *X. orzyae*[25] and *Y. pestis*[26] FabV structures, there were no structural homologues with a sufficiently high degree of similarity to tdTer to use as search models for molecular replacement. Therefore, the initial model for tdTer was built with phasing determined from a two-wavelength MAD data set of selenomethionine-substituted protein, with the most complete monomer serving as the molecular replacement model for the additional tdTer chains in the asymmetric unit [root-mean-square deviation (rmsd), 0.170–0.256 Å between monomers]. Electron density was identified for all 401 native residues in each of the monomers but was not observed for the N-terminal GTGA linker, which was not included in the model. The crystal structure of native tdTer was then determined to 2.00 Å resolution by molecular replacement using the selenomethionine-modified structure and found to be in close agreement (rmsd, 0.246 Å for a single monomer) (Table 1).

dx.doi.org/10.1021/bi300879n | *Biochemistry* 2012, 51, 6827–6837

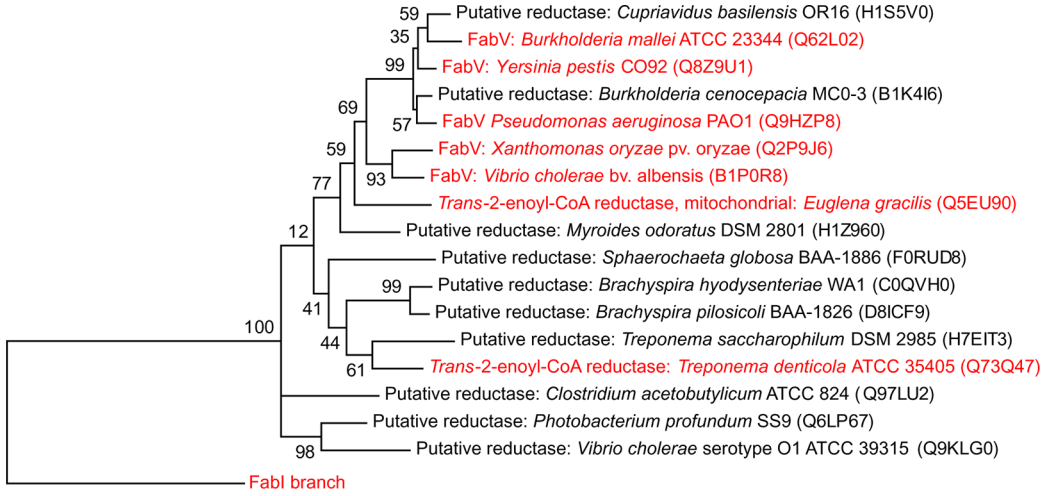

Figure 1. Phylogenetic tree of Ter, FabV, and FabI homologues. Maximum likelihood analysis of characterized Ter, FabV, and FabI enzymes (red) and homologues with <50% identical sequences from the UniRef50 database. Bootstrap values are indicated at branch points.

Table 1. Data Collection and Refinement Statistics for GTGA-Ter Structures

	selenomethionine tdTer[a]		tdTer
Data Collection			
space group	*P*1	*P*1	*P*1
unit cell parameters			
a, *b*, *c* (Å)	62.7, 87.6, 92.4	62.4, 87.6, 91.6	62.05, 87.05, 91.46
α, *β*, *γ* (deg)	106.4, 109.6, 98.3	106.3, 109.9, 98.4	106.14, 109.72, 98.52
wavelength (Å)	0.979	0.957 (Se remote)	1.116
resolution (Å)	19.85−2.05 (2.12−2.05)	19.85−2.05 (2.12−22.05)	19.68−2.00 (2.071−2.00)
R_{merge} (%)	15.1 (59.9)	16.9 (72.8)	13.5 (69.9)
$\langle I/\sigma(I)\rangle$	20.67 (4.38)	13.29 (2.77)	15.61 (2.60)
total no. of reflections	438763 (70586)	472313 (75927)	222904 (14852)
no. of unique reflections	114220 (17931)	122645 (19279)	105852 (7127)
completeness (%)	97.1 (96.1)	97.4 (96.0)	94.04 (88.17)
multiplicity	3.8 (3.9)	3.9 (3.9)	2.1 (2.1)
Refinement			
R_{work} (%)	18.22 (23.92)		20.62 (30.66)
R_{free} (%)	21.45 (27.29)		23.47 (35.02)
no. of atoms	12861		12957
nonsolvent	12316		12316
solvent	545		641
B factor	39.90		37.70
protein	39.90		37.70
water	41.20		37.90
rmsd			
bond lengths (Å)	0.004		0.003
bond angles (deg)	0.78		0.66
Ramachandran plot (%)			
most favored	98		97
disallowed	0		0.25
PDB entry	4GGP		4GGO

[a]Selenomethionine tdTer data sets were merged to build the model.

The tdTer structure contains 15 *α*-helices and 10 *β*-strands comprising one six-stranded parallel *β*-sheet (strands 1−4, 9, and 10) and two two-stranded antiparallel *β*-sheets (strands 5 and 6 and strands 7 and 8) (Figure 2A). Like other members of the SDR family, tdTer possesses a typical Rossman fold for nucleotide binding based on the presence of the G69-X-G71-XXXX-G76 consensus motif. In the crystal structure, the Rossman fold is formed by helices 3 and 5 along with the six-stranded *β*-sheet and contains E80 in the cofactor binding pocket (Figure 2A and Figure S4 of the Supporting Information), predicting specificity for NADH over NADPH,[37−39] which is consistent with previous biochemical studies of tdTer.[13] The active site can be located by the putative catalytic tyrosine, Y240 (Figure 2B); however, several reductases along the tdTer branch, including tdTer, contain both a Y-X_8-K and a Y-X_6-K consensus sequence that are the respective signatures of FabVs[23] and the other more common families of enoyl-ACP reductases, such as FabI, FabK, and

dx.doi.org/10.1021/bi300879n | *Biochemistry* 2012, 51, 6827−6837

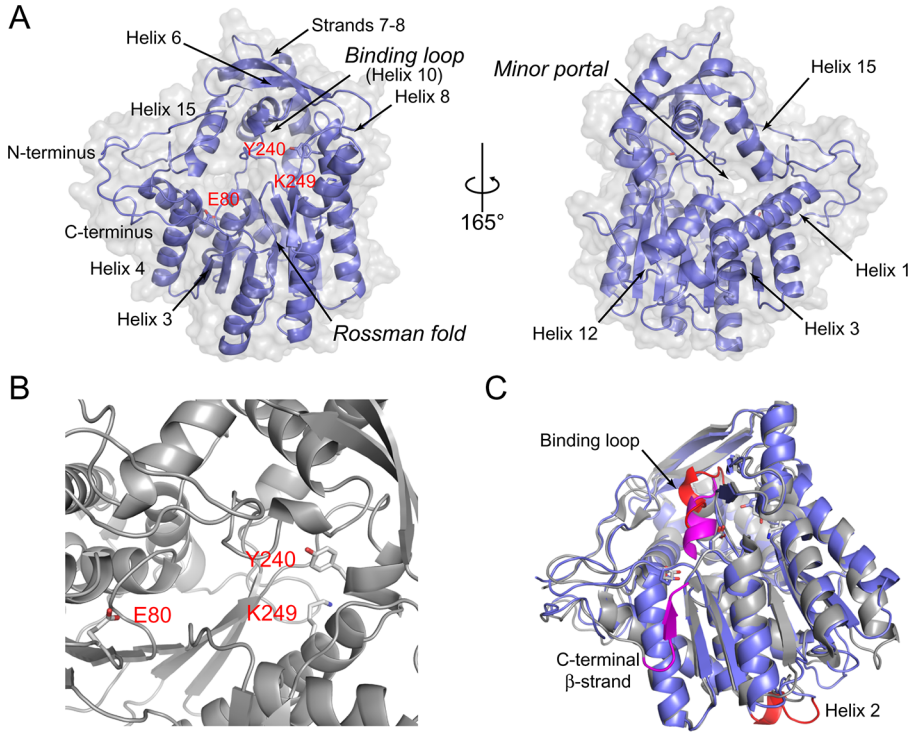

Figure 2. Crystal structure of tdTer. (A) Cartoon representation of tdTer looking down at the active site (Y240 and K249) and Rossman fold (E80) as well as a view rotated 165° around the *y*-axis. The major (helices 3, 4, 6, 8−10, and 15 and strands 7 and 8) and minor (helices 1, 3, 12, and 15) portals and the substrate binding loop (residues T278−V286, including helix 10) are indicated. (B) View of the putative active site showing Y240 and K249 as well as E80 and the NADH binding pocket formed by the Rossman fold. (C) Overlay of the tdTer crystal structure (blue) with the FabV from *Y. pestis* (gray). The differences in the main chain trace are highlighted in red (tdTer) or magenta (FabV).

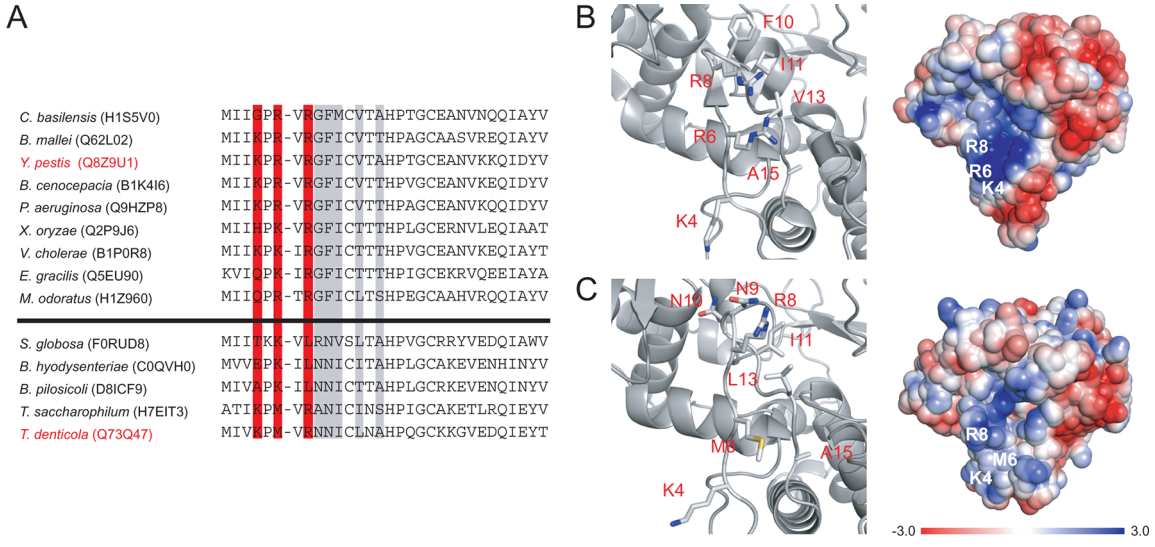

Figure 3. Comparison of the ACP binding site of FabV from *Y. pestis* compared to tdTer. (A) Sequence alignments of the N-terminal region of FabVs and Ters involved in ACP recognition. (B) View and electrostatic map of the ACP binding surface of FabV. The electrostatic map was generated by APBS in PyMOL with the scale indicating the calculated potential in solution. (C) View and electrostatic map of the same region of tdTer.

FabL.[40] From the relative orientations of K247 and K249 (Figure S5 of the Supporting Information), tdTer appears to share the FabV consensus sequence as the side chain of K249 is directed into rather than away from the active site. On the basis of the similarity in active site architecture, tdTer also may also share the resistance to triclosan inhibition as observed for FabVs.[22−24,26] Surrounding the active site, tdTer also has the major (helices 3, 4, 6, 8−10, and 15 and strands 7 and 8) and minor (helices 1, 3, 12, and 15) portals into the active site and substrate binding loop (residues T278−V286, including helix 10) that are shared with structurally characterized FabVs and FabIs.

Overall, the tdTer structure aligns well at the structural level with the recently reported FabV structures from *X. orzyae* (rmsd, 0.630 Å) and *Y. pestis* (rmsd, 0.691 Å) (Figure 2C). One of the main differences in the main chain trace of tdTer is the

dx.doi.org/10.1021/bi300879n | *Biochemistry* 2012, 51, 6827−6837

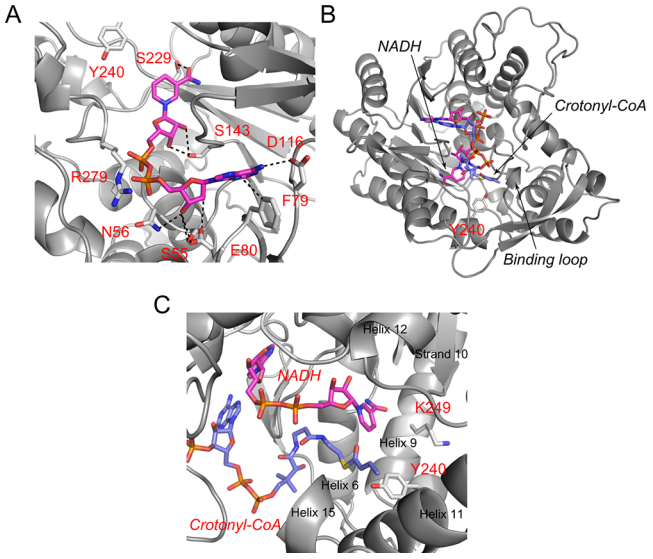

Figure 4. Docking model of tdTer bound to NADH and crotonyl-CoA. (A) Initial model of tdTer with the docked NADH redox cofactor (magenta). Dotted lines represent distances of <4 Å. (B) Docking model of the tdTer ternary complex with NADH (magenta) and crotonyl-CoA (blue). (C) View of the terminal carbon of the crotonyl-CoA acyl group (blue) with respect to the minor portal.

absence of the final β-strand at the C-terminus found in the FabVs that forms part of the β-sheet in the Rossman fold (Figure 2C). These residues are situated directly next to the binding pocket for the adenine moiety of NADH but do not appear to directly interact with the cofactor. The tdTer structure also contains an elongated loop (T40−K48), with an α-helix (helix 2) that is missing from the FabV structures. Although this loop is distal to the substrate binding pocket, it connects helix 1 to the six-stranded β-sheet and may play a role in the movement of one of the α-helices (helix 1) of the minor portal. In addition to these differences, there is a 3.3 Å shift in the substrate binding loop away from the minor portal that increases the size of the binding pocket in the tdTer structure compared to those of the FabV structures.

One possible functional difference between Ters and FabVs is that the Ter enzymes are proposed to be part of a FAS system that relies on CoA rather than ACPs,[17,21] which serve as the acyl carrier in canonical type II FAS systems. The interaction of ACPs with the enzymes involved in fatty acid biosynthesis is mediated by the N-terminal α-helix of the ACP that contains negatively charged residues surrounded by a hydrophobic region and associates with the corresponding positively charged patch on its protein partners that is also surrounded by hydrophobic residues.[41−43] In *Y. pestis* FabV, the ACP recognition domain is suggested to consist of basic residues K4, R6, and R8 and hydrophobic residues G9, F10, I11, V13, and A15 at the N-terminus.[26] In comparison, reductases in the tdTer branch lack the full complement of basic residues, and several of the proposed hydrophobic areas are replaced with charged or polar residues instead (Figure 3A). For tdTer specifically, K4 and R8 overlay well with the corresponding residues in FabV but the exchange of R6 for M6 results in the formation of a hydrophobic center in this charged patch and a significant decrease in the positive charge at the surface (Figure 3B,C). In addition, G9 and F10 in the hydrophobic region are changed to polar amino acids, N9 and N10, respectively, thereby reducing the hydrophobicity of the N-terminal region of tdTer. Taken together, these changes

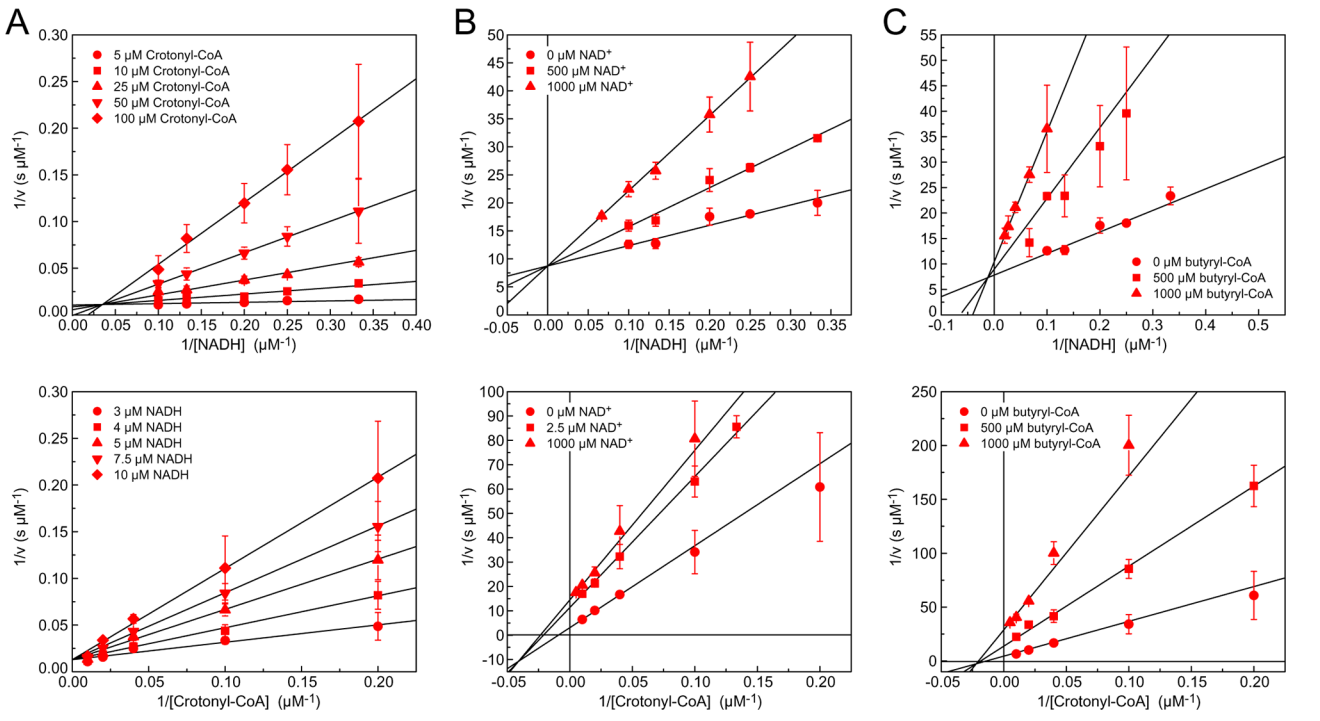

Figure 5. Steady-state kinetic characterization of tdTer. (A) Double-reciprocal plots with varying NADH and crotonyl-CoA concentrations indicate ternary complex formation. (B) Double-reciprocal plots monitoring NAD^+ product inhibition with respect to NADH (top) and crotonyl-coA (bottom). Data are fit to a linear regression and represent means ± the standard deviation ($n \geq 3$). (C) Double-reciprocal plots monitoring butyryl-CoA product inhibtion with respect to NADH (top) and crotonyl-CoA (bottom). Data are fit to a linear regression and represent means ± the standard deviation ($n \geq 3$).

dx.doi.org/10.1021/bi300879n | *Biochemistry* 2012, 51, 6827−6837

Table 2. Kinetic Constants Measured for Enoyl-CoA Reduction by Wild-Type and Mutant TdTers[a]

	crotonyl-CoA			hexenoyl-CoA			C_6:C_4
enzyme	k_{cat} (s^{-1})	K_M (μM)	k_{cat}/K_M (M^{-1} s^{-1})	k_{cat} (s^{-1})	K_M (μM)	k_{cat}/K_M (M^{-1} s^{-1})	k_{cat}/K_M ratio
wild type	91 ± 4	70 ± 10	(1.3 ± 0.2) × 10^6	112 ± 5	12 ± 2	(9 ± 2) × 10^6	7 ± 2
Y240F	0.73 ± 0.02[b]	49 ± 4	(1.5 ± 0.1) × 10^4	nd[c]	nd[c]	nd[c]	nd[c]
I287A	7.1 ± 0.8	160 ± 50	(4 ± 1) × 10^4	15.3 ± 0.6	3.4 ± 0.6	(4.5 ± 0.8) × 10^6	100 ± 40
L291A	37 ± 3	110 ± 30	(3 ± 1) × 10^5	50 ± 2	38 ± 4	(1.3 ± 0.2) × 10^6	4 ± 1
F295A	73 ± 4	100 ± 20	(7 ± 1) × 10^5	64 ± 3	19 ± 2	(3.4 ± 0.4) × 10^6	5 ± 1
Y370A	92 ± 6	150 ± 30	(6 ± 1) × 10^5	48 ± 4	18 ± 5	(2.7 ± 0.8) × 10^6	4 ± 2
L276A/V277A	15.6 ± 0.2	60 ± 10	(2.6 ± 0.5) × 10^5	19 ± 3	7 ± 3	(3 ± 1) × 10^6	11 ± 5
L276A/V277A/F295A	18.9 ± 0.4	210 ± 20	(8.9 ± 0.7) × 10^4	22.4 ± 0.6	15 ± 1	(1.5 ± 0.1) × 10^6	17 ± 2

	dodecenoyl-CoA		
enzyme	k_{cat} (s^{-1})	K_M (μM)	k_{cat}/K_M (M^{-1} s^{-1})
wild type	90 ± 10	3 ± 1	(3 ± 1) × 10^7
Y240F	nd[c]	nd[c]	nd[c]
I287A	6 ± 2	4 ± 2	(2 ± 1) × 10^6
L291A	nd[c]	nd[c]	nd[c]
F295A	nd[c]	nd[c]	nd[c]
Y370A	nd[c]	nd[c]	nd[c]
L276A/V277A	nd[c]	nd[c]	nd[c]
L276A/V277A/F295A	24 ± 1	1.1 ± 0.3	(2.1 ± 0.5) × 10^7

[a]Data are means ± the standard error ($n \geq 3$) as determined from nonlinear curve fitting. The error in the k_{cat}/K_M parameter was obtained from propagation of the error from the individual kinetic terms. [b]Y240F kinetic parameters were measured with 200 mM NADH; all other parameters were measured with 100 mM NADH. [c]Not determined.

Table 3. Inhibition of Hexanoyl-CoA and Lauroyl-CoA on Wild-Type and Mutant TdTers[a]

enzyme	inhibitor	[inhibitor] (μM)	K_i (μM)	K_i' (μM)
wild type	butyryl-CoA	500	400 ± 100	750 ± 60
		1000	400 ± 100	4100 ± 400
	hexanoyl-CoA	50	50 ± 10	110 ± 10
		250	80 ± 30	250 ± 30
	lauroyl-CoA	1	0.5 ± 0.1	3.1 ± 0.2
		1.5	0.4 ± 0.1	3.7 ± 0.5
I287A	lauroyl-CoA	0.025	0.06 ± 0.02	0.53 ± 0.08
		0.1	0.03 ± 0.02	0.23 ± 0.06
L276A/V277A/F295A	lauroyl-CoA	5	10 ± 2	12 ± 1
		10	3 ± 1	5.6 ± 0.8

[a]Data are means ± the standard error ($n \geq 3$) as determined from nonlinear curve fitting. Errors in K_i and K_i' were obtained from propagation of the error from the individual kinetic terms.

could lead to a difference in acyl carrier specificity between the Ter and FabV families.

Docking Model for NADH and Enoyl-CoA Binding. A docking model was generated to examine how the enoyl-CoA substrate and NADH cofactor might be oriented within the tdTer active site. The structures of the substrates were first minimized and then docked as flexible ligands using Glide.[33−35,44] The initial model was generated with NADH alone, as there are a significant number of crystal structures determined with a nicotinamide cofactor bound to a Rossman fold that could be used for model validation. The top five binding models were examined (Figure S6 of the Supporting Information) with the top four models placing the nicotinamide in the predicted binding pocket with N^6 of the adenine within hydrogen bonding distance of D116 and the 3′-OH of the ribose sugar bound to E80. These results agree with the NADH binding mode found in other structures containing a Rossman fold, including the *Y. pestis* FabV. The second solution was selected for docking of the enoyl-CoA substrate because it was the most similar to the FabV structure with the nicotinamide ring adjacent to Y240 (Figure 4A and Figure S6 of the Supporting Information).

The C_4 substrate, crotonyl-CoA, which was previously reported to be the major substrate for tdTer,[13] was then docked into the tdTer−NADH model using the same approach. In this case, the full acyl-CoA substrate and the substrate without the adenine or adenosine moiety were used for docking studies to control for the lack of adenosine-specific interactions typical of many CoA binding enzymes.[45,46] Regardless of the ligand, all models place the double bond of the butenoyl functional group between the docked NADH substrate and Y240 and the terminal carbon of the acyl group at the entrance to the minor portal near a tightly packed area formed by a strand containing G278−V280 and helix 11 (Figure 4B,C and Figure S7 of the Supporting Information). Docking was also attempted with longer enoyl-CoA substrates but did not yield any models with substrate bound within the active site. We then used MOLE[47] to further examine the minor portal of tdTer and the FabVs from *X. orzyae* and *Y. pestis* to explore how these substrates might be accommodated. These studies show that while the minor portal is open in all

dx.doi.org/10.1021/bi300879n | *Biochemistry* 2012, 51, 6827−6837

three structures, it contains significant bottlenecks of 1.5−2 Å that would prevent binding of substrates larger than crotonyl-CoA to a static structure. A conformational change or dynamic movement in the minor portal would therefore be necessary to allow tdTer to interact with these substrates if they were to bind with the acyl moiety in the minor portal of the enzyme.

Biochemical Characterization of Ter. Enzymes that catalyze reactions similar to those of tdTer, including the FabV from *B. mallei*,[23] have generally been found to form a ternary complex using an ordered bi-bi reaction mechanism in which the redox cofactor is bound first followed by the enoyl-CoA substrate.[48−51]The docking model of tdTer with NADH and crotonyl-CoA appears to support this mechanism, as the binding site of NADH would be occluded if crotonyl-CoA were to bind first. Steady-state kinetic experiments with varying NADH and crotonyl-CoA concentrations confirm the formation of a ternary complex, with the double-reciprocal plots showing a set of intersecting lines (Figure 5A). The selectivity of tdTer for NADH [K_M = 5.2 ± 0.4 μM; k_{cat}/K_M = (1.6 ± 0.1) × 10^7 M^{-1} s^{-1}] over NADPH [K_M = 190 ± 20 μM; k_{cat}/K_M = (3.9 ± 0.5) × 10^5 M^{-1} s^{-1}] was also confirmed at this time. The order of binding was then established by examining the effect of product inhibition on the steady-state kinetics. These studies show that NAD^+ acts as a competitive inhibitor for NADH binding and a mixed inhibitor with respect to crotonyl-CoA (Figure 5B), while butyryl-CoA serves as a mixed inhibitor of both substrates (Figure 5C). This pattern of product inhibition indicates that tdTer also uses an ordered bi-bi reaction mechanism with NADH binding first.

We next turned our attention to mutagenesis studies to elucidate the function of the putative catalytic tyrosine, Y240, as well as residues that might be involved in substrate selectivity. Introduction of the Y240F mutation leads to a 5000-fold decrease in catalytic efficiency with no significant change in K_M (Table 2), which is consistent with a key role in catalysis as suggested for FabVs[23,26] and FabIs.[10,49,52] In terms of substrate specificity, the k_{cat}/K_M of tdTer for crotonyl-CoA is similar to the value measured for the FabV from *V. cholerae*[22] (Table 2). These data are consistent with the proposal that Ters can service CoA-dependent FAS pathways; however, their activity with ACP-dependent substrates has not yet been fully explored.

Although tdTer had previously been reported to exclude the hexenoyl-CoA substrate,[13] it has been used in the construction of synthetic fuel pathways for hexanol production, which shows that it is active *in vivo* on a C_6 substrate.[53] Indeed, we find that tdTer is 7- and 25-fold more active *in vitro* with hexenoyl-CoA and dodecenoyl-CoA, respectively, as a result of both higher k_{cat} values and lower K_M values. With this result in hand, we decided to explore the role of the substrate binding loop in influencing chain length specificity. The I287A, L291A, F295A, Y370A, L276A/V277A, and L276A/V277A/F295A mutations were selected because these residues appear to be involved in mediating the conformation of the binding loop (Figure S8 of the Supporting Information). Three of the mutants, L291A, F295A, and Y370A, demonstrated kinetic behavior relatively similar to that of wild-type tdTer on crotonyl-CoA and hexenoyl-CoA (Table 2). Because of the significant decreases in k_{cat} with the remaining three mutants, I287A, L276A/V277A, and L276A/V277A/F295A, the data were normalized by calculating the k_{cat}/K_M ratios for the C_4 versus C_6 substrate for each individual mutant. Using this analysis, we see that both the I287A single mutant and the L276A/V277A/F295A triple mutant exhibit larger increases in catalytic efficiency on the longer hexenoyl-CoA substrate of 100- and 17-fold compared to that of the wild type (7-fold). These results suggest that these mutations may increase the accessibility of the longer acyl chain to the active site pocket through perturbations of either the minor or major portal, each of which is modulated by the substrate binding loop.

In addition to demonstrating higher catalytic efficiencies and lower K_M values, the longer chain substrates also cause a significant level of inhibition of tdTer under saturating conditions. Neither hexenoyl-CoA nor dodecenoyl-CoA changes $K_{M,NADH}$, which shows that the longer chain acyl-CoA substrates do not compete with NADH binding (Figure S9 of the Supporting Information). In contrast, we observe strong product inhibition with the addition of hexanoyl-CoA and lauroyl-CoA (Table 3 and Figure S10 of the Supporting Information). The data were fit to a model for mixed inhibition based on the patterns observed in the double-reciprocal plot where both k_{cat} and K_M are affected. Because of the order of binding as well as the absence substrate inhibition, which is consistent with previous studies,[23] we interpret these data to mean that the acyl-CoA product can bind either tdTer-NADH or tdTer-NAD^+. The two mutants with higher C_6:C_4 ratios of activity, I287A and L276A/V277A/F295A, were also characterized with respect to product inhibition by lauroyl-CoA (Table 3 and Figure S10 of the Supporting Information). Interestingly, K_i and K_i' are much lower than that of the wild type for the I287A mutant but not the triple mutant. The correlation of C_{12} product inhibition with the increased C_6:C_4 activity ratio for the I287A mutation, which is located near the front of the binding loop, seems to suggest that the major portal is more important than the minor portal for recognition of longer chain substrates. In comparison, the weak preference of the L276A/V277A/F295A mutant for the C_6 substrate along with the higher K_i and K_i' versus wild-type tdTer seems to imply that relaxing of the minor portal can accommodate slightly larger substrates without increasing the affinity for an extended acyl chain.

CONCLUSIONS

Enoyl-ACP (CoA) reductases catalyze a key step in the biosynthesis of reduced hydrocarbons and are important for driving the pathway equilibrium forward toward chain elongation. The diversity of isozymes available for this reaction is interesting with regard to the evolution of different FAS systems as well as the engineering of pathways to produce advanced biofuels. In this work, we have biochemically and structurally characterized a member of the Ter family of reductases, which is proposed to participate in CoA-dependent rather than ACP-dependent pathways.[21] Although the Ters are distinct from the FabI, FabK, and FabL enoyl-ACP reductase isozymes, they are highly related to the FabV family based on their close phylogeny as well as their structural similarity. One interesting difference between the tdTer structure and the FabV structures from *X. orzyae* and *Y. pestis* is the difference in the ACP binding surface, which may lead to differences in acyl carrier specificity. However, it would not be surprising if Ters are competent to reduce both CoA- and ACP-linked substrates.

Initial characterization of tdTer indicates that Y240 is the catalytic tyrosine and that K249 is likely the active site lysine shared by FabVs and FabIs. Further biochemical studies show that tdTer prefers NADH over NADPH and uses an ordered bi-bi mechanism initiated by binding of the redox cofactor. Although tdTer had been previously reported to prefer C_4

substrates,[13] we observe that the catalytic efficiency is higher on both C_6 and C_{12} substrates. The strong product inhibition of wild-type and mutant Ters implies that the hydrocarbon tail of the substrate is important for binding and recognition. Preliminary mutagenesis experiments reveal that the substrate binding loop appears to be involved in determining chain length specificity through changes in either the minor or the major portal. We have identified two mutants, I287A and I276A/V277A/F295A, that demonstrate a stronger preference for C_6 over C_4 substrates than the wild type. In this regard, the strong impact of the I287A mutation, which is located near the front of the major portal, on interaction with both C_6 and C_{12} acyl-CoAs could be consistent with the binding mode observed in FabI structures.[54]

■ ASSOCIATED CONTENT

Supporting Information

Conditions for steady-state kinetic measurements, conditions for order of binding experiments, conditions for product inhibition experiments, list of oligonucleotides, SDS−PAGE gels, size-exclusion chromatograms, additional structure figures, and additional steady-state kinetic data. This material is available free of charge via the Internet at http://pubs.acs.org.

Accession Codes

The atomic coordinates and structure factors for the structures reported herein have been deposited in the Protein Data Bank as entries 4GGO and 4GGP.

■ AUTHOR INFORMATION

Corresponding Author

*E-mail: mcchang@berkeley.edu. Telephone: (510) 642-8545. Fax: (510) 642-9863.

Author Contributions

B.B.B.-W. conducted all experiments. A.M.W. assisted in the analysis of data. B.B.B.-W., A.M.W., and M.C.Y.C. designed the experiments and wrote the manuscript.

Funding

This work was funded by the generous support of a National Science Foundation CAREER award (CHE-0548245) and by the Aldo DeBenedictis and Chevron Predoctoral Fellowships to B.B.B.-W. A.M.W. acknowledges the support of a National Institutes of Health NRSA Training Grant (1 T32 GMO66698) and a National Science Foundation Graduate Research Fellowship. The Advanced Light Source is supported by the U.S. Department of Energy under Contract DEAC02-05CH11231.

Notes

The authors declare no competing financial interest.

■ ACKNOWLEDGMENTS

We thank James Holton and George Meigs (beamline 8.3.1, Advanced Light Source, Lawrence Berkeley National Laboratory) and Kathy Durkin (University of California, Berkeley, CA) for assistance with X-ray data collection and molecular modeling, respectively, as well as Jonathan Winger and Tiago Barros in the Kuriyan laboratory (University of California, Berkeley, CA) for helpful discussions.

■ ABBREVIATIONS

ACP, acyl carrier protein; CoA, coenzyme A; cv, column volumes; FAS, fatty acid synthase; MAD, multiwavelength anomalous diffraction; NAD(H), nicotinamide adenine dinucleotide; NADP(H), nicotinamide adenine dinucleotide phosphate; Ter, *trans*-enoyl-CoA reductase; TEV, tobacco etch virus.

■ REFERENCES

(1) Luckey, M. (2008) *Membrane structural biology: With biochemical and biophysical foundations*, Cambridge University Press, Cambridge, U.K.

(2) Simons, K. (2011) in *Cold Spring Harbor Perspectives in Biology*, Cold Spring Harbor Laboratory Press, Woodbury, NY.

(3) Lu, X., Vora, H., and Khosla, C. (2008) Overproduction of free fatty acids in *E. coli*: Implications for biodiesel production. *Metab. Eng. 10*, 333−339.

(4) Steen, E. J., Kang, Y., Bokinsky, G., Hu, Z., Schirmer, A., McClure, A., Del Cardayre, S. B., and Keasling, J. D. (2010) Microbial production of fatty-acid-derived fuels and chemicals from plant biomass. *Nature 463*, 559−562.

(5) Schirmer, A., Rude, M. A., Li, X., Popova, E., and del Cardayre, S. B. (2010) Microbial biosynthesis of alkanes. *Science 329*, 559−562.

(6) Chisti, Y. (2007) Biodiesel from microalgae. *Biotechnol. Adv. 25*, 294−306.

(7) Hu, Q., Sommerfeld, M., Jarvis, E., Ghirardi, M., Posewitz, M., Seibert, M., and Darzins, A. (2008) Microalgal triacylglycerols as feedstocks for biofuel production: Perspectives and advances. *Plant J. 54*, 621−639.

(8) Meng, X., Yang, J., Xu, X., Zhang, L., Nie, Q., and Xian, M. (2009) Biodiesel production from oleaginous microorganisms. *Renewable Energy 34*, 1−5.

(9) Rock, C. O., and Cronan, J. E. (1996) *Escherichia coli* as a model for the regulation of dissociable (type II) fatty acid biosynthesis. *Biochim. Biophys. Acta 1302*, 1−16.

(10) White, S. W., Zheng, J., Zhang, Y. M., and Rock, C. O. (2005) The structural biology of type II fatty acid biosynthesis. *Annu. Rev. Biochem. 74*, 791−831.

(11) Schweizer, E., and Hofmann, J. (2004) Microbial type I fatty acid synthases (FAS): Major players in a network of cellular FAS systems. *Microbiol. Mol. Biol. Rev. 68*, 501−517.

(12) Asturias, F. J., Chadick, J. Z., Cheung, I. K., Stark, H., Witkowski, A., Joshi, A. K., and Smith, S. (2005) Structure and molecular organization of mammalian fatty acid synthase. *Nat. Struct. Mol. Biol. 12*, 225−232.

(13) Tucci, S., and Martin, W. (2007) A novel prokaryotic trans-2-enoyl-CoA reductase from the spirochete *Treponema denticola*. *FEBS Lett. 581*, 1561−1566.

(14) Bond-Watts, B. B., Bellerose, R. J., and Chang, M. C. (2011) Enzyme mechanism as a kinetic control element for designing synthetic biofuel pathways. *Nat. Chem. Biol. 7*, 222−227.

(15) Shen, C. R., Lan, E. I., Dekishima, Y., Baez, A., Cho, K. M., and Liao, J. C. (2011) Driving forces enable high-titer anaerobic 1-butanol synthesis in *Escherichia coli*. *Appl. Environ. Microbiol. 77*, 2905−2915.

(16) Inui, H., Miyatake, K., Nakano, Y., and Kitaoka, S. (1982) Wax ester fermentation in *Euglena gracilis*. *FEBS Lett. 150*, 89−93.

(17) Inui, H., Miyatake, K., Nakano, Y., and Kitaoka, S. (1984) Fatty acid synthesis in mitochondria of *Euglena gracilis*. *Eur. J. Biochem. 142*, 121−126.

(18) Inui, H., Miyatake, K., Nakano, Y., and Kitaoka, S. (1985) The physiological role of oxygen-sensitive pyruvate dehydrogenase in mitochondrial fatty acid synthesis in *Euglena gracilis*. *Arch. Biochem. Biophys. 237*, 423−429.

(19) Tucci, S., Vacula, R., Krajcovic, J., Proksch, P., and Martin, W. (2010) Variability of wax ester fermentation in natural and bleached *Euglena gracilis* strains in response to oxygen and the elongase inhibitor flufenacet. *J. Eukaryotic Microbiol. 57*, 63−69.

(20) Inui, H., Miyatake, K., Nakano, Y., and Kitaoka, S. (1986) Purification and some properties of short chain-length specific trans-2-enoyl-CoA reductase in mitochondria of *Euglena gracilis*. *J. Biochem. 100*, 995−1000.

(21) Hoffmeister, M., Piotrowski, M., Nowitzki, U., and Martin, W. (2005) Mitochondrial trans-2-enoyl-CoA reductase of wax ester fermentation from *Euglena gracilis* defines a new family of enzymes involved in lipid synthesis. *J. Biol. Chem. 280*, 4329−4338.
(22) Massengo-Tiasse, R. P., and Cronan, J. E. (2008) *Vibrio cholerae* FabV defines a new class of enoyl-acyl carrier protein reductase. *J. Biol. Chem. 283*, 1308−1316.
(23) Lu, H., and Tonge, P. J. (2010) Mechanism and inhibition of the FabV enoyl-ACP reductase from *Burkholderia mallei*. *Biochemistry 49*, 1281−1289.
(24) Zhu, L., Lin, J., Ma, J., Cronan, J. E., and Wang, H. (2010) Triclosan resistance of *Pseudomonas aeruginosa* PAO1 is due to FabV, a triclosan-resistant enoyl-acyl carrier protein reductase. *Antimicrob. Agents Chemother. 54*, 689−698.
(25) Li, H., Zhang, X., Bi, L., He, J., and Jiang, T. (2011) Determination of the crystal structure and active residues of FabV, the enoyl-ACP reductase from *Xanthomonas oryzae*. *PLoS One 6*, e26743.
(26) Hirschbeck, M. W., Kuper, J., Lu, H., Liu, N., Neckles, C., Shah, S., Wagner, S., Sotriffer, C. A., Tonge, P. J., and Kisker, C. (2012) Structure of the *Yersinia pestis* FabV enoyl-ACP reductase and its interaction with two 2-pyridone inhibitors. *Structure 20*, 89−100.
(27) Li, W., Jaroszewski, L., and Godzik, A. (2001) Clustering of highly homologous sequences to reduce the size of large protein databases. *Bioinformatics 17*, 282−283.
(28) Consortium, T. U. (2012) Reorganizing the protein space at the Universal Protein Resource (UniProt). *Nucleic Acids Res. 40*, D71−D75.
(29) Tamura, K., Peterson, D., Peterson, N., Stecher, G., Nei, M., and Kumar, S. (2011) MEGA5: Molecular evolutionary genetics analysis using maximum likelihood, evolutionary distance, and maximum parsimony methods. *Mol. Biol. Evol. 28*, 2731−2739.
(30) Edgar, R. C. (2004) MUSCLE: Multiple sequence alignment with high accuracy and high throughput. *Nucleic Acids Res. 32*, 1792−1797.
(31) Adams, P. D., Afonine, P. V., Bunkoczi, G., Chen, V. B., Davis, I. W., Echols, N., Headd, J. J., Hung, L.-W., Kapral, G. J., Grosse-Kunstleve, R. W., McCoy, A. J., Moriarty, N. W., Oeffner, R., Read, R. J., Richardson, D. C., Richardson, J. S., Terwilliger, T. C., and Zwart, P. H. (2010) PHENIX: A comprehensive Python-based system for macromolecular structure solution. *Acta Crystallogr. D66*, 213−221.
(32) Emsley, P., and Cowtan, K. (2004) Coot: Model-building tools for molecular graphics. *Acta Crystallogr. D60*, 2126−2132.
(33) Friesner, R. A., Banks, J. L., Murphy, R. B., Halgren, T. A., Klicic, J. J., Mainz, D. T., Repasky, M. P., Knoll, E. H., Shelley, M., Perry, J. K., Shaw, D. E., Francis, P., and Shenkin, P. S. (2004) Glide: A new approach for rapid, accurate docking and scoring. 1. Method and assessment of docking accuracy. *J. Med. Chem. 47*, 1739−1749.
(34) Halgren, T. A., Murphy, R. B., Friesner, R. A., Beard, H. S., Frye, L. L., Pollard, W. T., and Banks, J. L. (2004) Glide: A new approach for rapid, accurate docking and scoring. 2. Enrichment factors in database screening. *J. Med. Chem. 47*, 1750−1759.
(35) Friesner, R. A., Murphy, R. B., Repasky, M. P., Frye, L. L., Greenwood, J. R., Halgren, T. A., Sanschagrin, P. C., and Mainz, D. T. (2006) Extra precision glide: Docking and scoring incorporating a model of hydrophobic enclosure for protein-ligand complexes. *J. Med. Chem. 49*, 6177−6196.
(36) Rasmussen, J. T., Borchers, T., and Knudsen, J. (1990) Comparison of the binding affinities of acyl-CoA-binding protein and fatty-acid-binding protein for long-chain acyl-CoA esters. *Biochem. J. 265*, 849−855.
(37) Scrutton, N. S., Berry, A., and Perham, R. N. (1990) Redesign of the coenzyme specificity of a dehydrogenase by protein engineering. *Nature 343*, 38−43.
(38) Perham, R. N., Scrutton, N. S., and Berry, A. (1991) New enzymes for old: Redesigning the coenzyme and substrate specificities of glutathione reductase. *BioEssays 13*, 515−525.
(39) Bocanegra, J. A., Scrutton, N. S., and Perham, R. N. (1993) Creation of an NADP-dependent pyruvate dehydrogenase multi-enzyme complex by protein engineering. *Biochemistry 32*, 2737−2740.
(40) Kim, K. H., Ha, B. H., Kim, S. J., Hong, S. K., Hwang, K. Y., and Kim, E. E. (2011) Crystal structures of enoyl-ACP reductases I (FabI) and III (FabL) from *B. subtilis*. *J. Mol. Biol. 406*, 403−415.
(41) Zhang, Y. M., Wu, B., Zheng, J., and Rock, C. O. (2003) Key residues responsible for acyl carrier protein and β-ketoacyl-acyl carrier protein reductase (FabG) interaction. *J. Biol. Chem. 278*, 52935−52943.
(42) Rafi, S., Novichenok, P., Kolappan, S., Zhang, X., Stratton, C. F., Rawat, R., Kisker, C., Simmerling, C., and Tonge, P. J. (2006) Structure of acyl carrier protein bound to FabI, the FASII enoyl reductase from *Escherichia coli*. *J. Biol. Chem. 281*, 39285−39293.
(43) Chan, D. I., and Vogel, H. J. (2010) Current understanding of fatty acid biosynthesis and the acyl carrier protein. *Biochem. J. 430*, 1−19.
(44) Repasky, M. P., Shelley, M., and Friesner, R. A. (2007) Flexible ligand docking with Glide. *Current Protocols in Bioinformatics 8*, Units 8−12.
(45) Barycki, J. J., O'Brien, L. K., Strauss, A. W., and Banaszak, L. J. (2000) Sequestration of the active site by interdomain shifting. Crystallographic and spectroscopic evidence for distinct conformations of L-3-hydroxyacyl-CoA dehydrogenase. *J. Biol. Chem. 275*, 27186−27196.
(46) Thoden, J. B., Holden, H. M., Zhuang, Z., and Dunaway-Mariano, D. (2002) X-ray crystallographic analyses of inhibitor and substrate complexes of wild-type and mutant 4-hydroxybenzoyl-CoA thioesterase. *J. Biol. Chem. 277*, 27468−27476.
(47) Petrek, M., Kosinova, P., Koca, J., and Otyepka, M. (2007) MOLE: A Voronoi diagram-based explorer of molecular channels, pores, and tunnels. *Structure 15*, 1357−1363.
(48) Wratten, C. C., and Cleland, W. W. (1963) Product inhibition studies on yeast and liver alcohol dehydrogenases. *Biochemistry 2*, 935−941.
(49) Parikh, S., Moynihan, D. P., Xiao, G., and Tonge, P. J. (1999) Roles of tyrosine 158 and lysine 165 in the catalytic mechanism of InhA, the enoyl-ACP reductase from *Mycobacterium tuberculosis*. *Biochemistry 38*, 13623−13634.
(50) Sahni-Arya, B., Flynn, M. J., Bergeron, L., Salyan, M. E., Pedicord, D. L., Golla, R., Ma, Z., Wang, H., Seethala, R., Wu, S. C., Li, J. J., Nayeem, A., Gates, C., Hamann, L. G., Gordon, D. A., and Blat, Y. (2007) Cofactor-specific modulation of 11β-hydroxysteroid dehydrogenase 1 inhibitor potency. *Biochim. Biophys. Acta 1774*, 1184−1191.
(51) Askonas, L. J., Ricigliano, J. W., and Penning, T. M. (1991) The kinetic mechanism catalysed by homogeneous rat liver 3α-hydroxysteroid dehydrogenase. Evidence for binary and ternary dead-end complexes containing non-steroidal anti-inflammatory drugs. *Biochem. J. 278*, 835−841.
(52) Rafferty, J. B., Simon, J. W., Baldock, C., Artymiuk, P. J., Baker, P. J., Stuitje, A. R., Slabas, A. R., and Rice, D. W. (1995) Common themes in redox chemistry emerge from the X-ray structure of oilseed rape (*Brassica napus*) enoyl acyl carrier protein reductase. *Structure 3*, 927−938.
(53) Dekishima, Y., Lan, E. I., Shen, C. R., Cho, K. M., and Liao, J. C. (2011) Extending carbon chain length of 1-butanol pathway for 1-hexanol synthesis from glucose by engineered *Escherichia coli*. *J. Am. Chem. Soc. 133*, 11399−11401.
(54) Rozwarski, D. A., Vilchèze, C., Sugantino, M., Bittman, R., and Sacchettini, J. C. (1999) Crystal structure of the *Mycobacterium tuberculosis* enoyl-ACP reductase, InhA, in complex with NAD^+ and a C16 fatty acyl substrate. *J. Biol. Chem. 274*, 15582−15589.